Journal of Tribology. Received April 13, 2023;
Accepted manuscript posted September 19, 2023. doi:10.1115/1.4064511

Investigation of the effect of underpressure between main and dust lip on the performance of radial shaft seals under instationary shaft movements

Yvo Stiemcke*
Chair of Machine Elements,
Gears and Tribology (MEGT)
Rheinland-Pfaelzische
Technische Universitaet
D-67663 Kaiserslautern
Germany
Email: yvo.stiemcke@rptu.de

Stefan Thielen
Chair of Machine Elements,
Gears and Tribology (MEGT)
Rheinland-Pfaelzische
Technische Universitaet
D-67663 Kaiserslautern
Germany
Email: stefan.thielen@rptu.de

Tim Schollmayer
Chair of Machine Elements,
Gears and Tribology (MEGT)
Rheinland-Pfaelzische
Technische Universitaet
D-67663 Kaiserslautern
Germany
Email: tim.schollmayer@rptu.de

Oliver Koch
Chair of Machine Elements,
Gears and Tribology (MEGT)
Rheinland-Pfaelzische
Technische Universitaet
D-67663 Kaiserslautern
Germany
Email: oliver.koch@rptu.de

ABSTRACT

Radial shaft seals (RSS) are increasingly used in applications with highly dynamic rotational shaft movement, high accelerations and frequent changes in rotational direction, e.g. positioning robots. For such instationary conditions, the behavior of radial shaft seals has not been adequately understood yet. Therefore, under such con-

*Address all correspondence to this author.

aitions, radial shaft seals show leakage much more frequently than under stationary conditions. This is a problem especially in food processing or surface treatment processes where even the smallest amount of oil leakage can cause significant financial and reputational damage. Previous investigations have shown, that leakage does mostly occur with shaft seals equipped with a contacting dust lip. Consequently, it is assumed, that the build up of negative pressure between dust and main lip plays a role in the leakage mechanism.

A measuring setup and evaluation strategy for measuring this underpressure during instationary shaft movements has been developed. A measurement regime with variation of different influential parameters has been conducted. Results show the build up of a much higher underpressure when compared to stationary shaft rotation with severe impacts on the RSS's operational behavior.

keywords: dust lip, leakage, positioning robots

Nomenclature

b_{DL} Contact width at dust lip / m

b_{ML} Contact width at main lip / m

h_f Spring offset from contact line / m

n Amount of Substance / mol

p_a Ambient pressure / Pa

p_d Differential pressure / Pa

p_i Internal pressure (cavity) / Pa

p_N Normal pressure / Pa

t Time / s

α Air side contact angle / °

β Oil side contact angle / °

φ_G Degree of greasing / .

R Gas constant / J/(mol·K)

T_i Internal temperature (cavity) / K

T_N Normal temperature / K

V_{DS} Dead volume of measurement system / m^3

V_{MS} Total volume of measurement system / m^3

V_{RSS} Cavity volume / m^3

Δp Load (Simulation) as pressurization / Pa

ΔT Temperature increment (Simulation) / K

$\Delta V/\Delta t$ Net flow rate / m^3/s

ϕ Swivel angle / °

1 Introduction

Radial shaft seals (RSS) are used to seal against a rotating shaft at its exit from lubricated machinery.

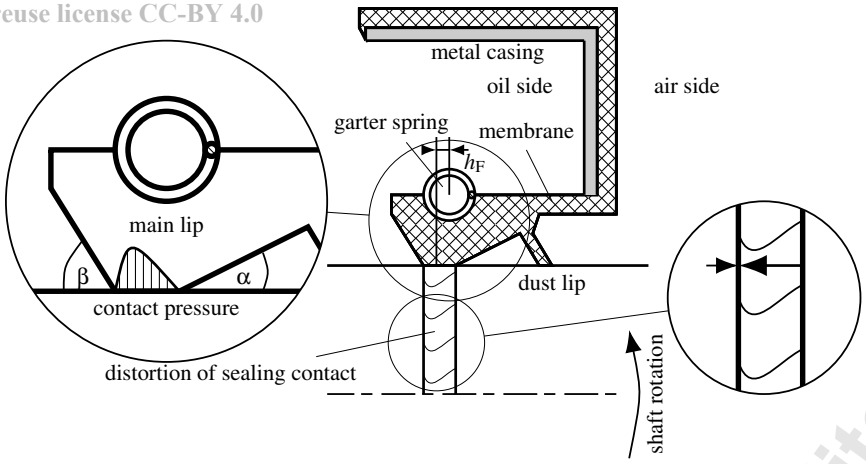

Fig. 1. Cross section of an assembled radial shaft seal with dust lip

They typically consist of a metal casing on which a rubber part is vulcanized (see Fig. 1). The rubber part includes a membrane and the (main) sealing lip itself. The inner diameter of the seal is smaller than the nominal shaft diameter. During assembly on the shaft, the seal is therefore widened and a contact pressure between shaft and seal is created. The lip usually is additionally loaded by a garter spring to ensure a minimum contact load when the rubber is softened at higher application temperatures [1]. The different angles on the air side (α) and oil side (β) as well as the distance between the plane of action of the garter spring and the sealing contact h_F ensure a skewed contact pressure distribution with its maximum closer to the oil side. The shaft rotation drags lubricant beneath the sealing contact and a lubrication film of approx. 1 µm is created between seal and shaft [2] [3]. The rough main lip is subsequently deformed in rotational direction, creating a pattern that is able to partly deflect the lubricant dragged in rotational direction towards the oil side. This mechanism is considered to be one of the main contributors to the sealing effect (reverse pumping effect) of RSS [4] [5].
When RSS are to be used in contaminated environments, a secondary lip, the dust lip, is employed which keeps dust and fluids away from the main lip. Typically, this dust lip is in contact with the shaft surface and thus exhibits a small reverse pumping effect directed towards the air side. To ensure proper lubrication of the dust lip, the cavity between main and dust lip is greased before assembly. Since both, the dust lip and the main lip actively pump out of this cavity, a negative pressure is built up. This suction effect significantly changes the contact angles, increases the radial force of the seal and thus the friction torque [6] [7].

1.1 Instationary shaft movements

In the past in most applications quasi-stationary shaft rotations with only small accelerations and infrequent changes of rotational direction were used. Therefore RSS have been developed and optimized for such scenarios. In recent years however, applications deviating from these conditions have become more relevant. Especially in production and drive technology, swiveling motions with swivel angles $\ll 360°$ and high frequency changes of rotational direction are more common. Examples for such applications are manufacturing, positioning or delta robots. The sealing mechanisms than guarantee reliable sealing in stationary conditions can be impaired by such movements.
In several cases, leakage has been reported for radial shaft seals used in delta robots or comparable applications, especially in combination with a contacting dust lip and a greased cavity between main and dust lip [8]. Under the same conditions, leakage did not occur for quasi-stationary shaft movements.
This proves to be a problem for both manufacturers and appliers of such robot systems. Especially in food processing [9] [10] [11] or surface treatment where even the smallest amount of lubricant leakage can cause severe financial and reputational damage.
Preliminary investigations of this phenomenon have shown, that leakage could only be provoked when using a contacting dust lip and reduced radial forces of the main lip (removal of garter spring) [8]. A venting of the cavity has been proposed as a first counter measure [8] and has shown good results in lab tests as well as in real applications. This suggests, that the build up of negative pressure between main and dust lip is involved in the failure mechanism. However, under certain conditions, a venting of the dust lip is not possible. For example in applications in the food processing industry, where regular cleaning with aggressive solvents, hot water and steam is necessary.
This motivates the investigation of the influence of negative pressures on the contact situation and sealing mechanism in RSS. In this contribution, we present experimental and simulative approaches and the results of in depth investigations on this phenomenon.

2 Methods

In this section, the measuring equipment used and the methods of the experimental as well as simulative investigation are described.

2.1 High acceleration test bench

The experimental studies on the behavior of rotary shaft seals at instationary shaft movement described in this article were carried out on a high acceleration test bench shown in Fig. 2.

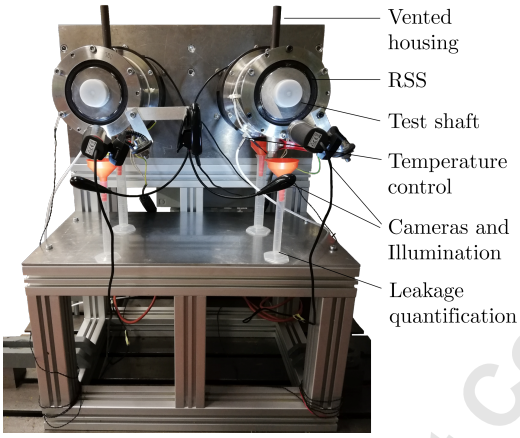

Fig. 2. High acceleration test bench

Mounted on a damping foundation for vibration decoupling from the environment, the test bench has two separately operating and identically constructed cells. In the application presented, both of them are vented. Oil sump temperature is controlled using a Pt100 screwed within the oil sump volume at the bottom of the cell and a silicone heating mat around the housing. Further systems for quantitative documentation of any leakage (collecting beakers below each housing cover in Fig. 2) as well as its time of appearance (digital cameras recording the sealing contact from the air side, see Fig. 2) are available. Fig. 3 shows the sectional view of a test cell in an exemplary test setup in detail.

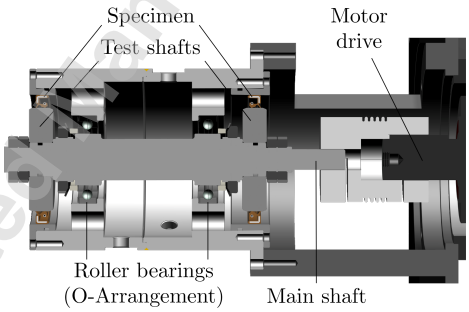

Fig. 3. Section view of a test cell

Mounted in the housing cover, two RSS can be tested simultaneously per cell. Two test shafts, each representing the seal countersurface, are fixed on a main shaft which can be driven directly by the motor.
Thus, the connected output can perform highly dynamic movement profiles with angular accelerations up to 8.500 rad/s^2. The current output angle and underlying drive data in addition to cell temperatures and pressure signals (see section 2.2) can be recorded at a sample rate of up to 4 kHz.
Furthermore, for operation at constant shaft speed, the frictional torque occuring at the sealing contact can be measured in a special configuration (not shown). Here, an in-line torque sensor (measurement range 0 to 1 Nm, linearity error $< 0.05\%$ F.S.) is installed between main shaft and motor drive instead of the coupling shown in Fig. 3. Thus, the total frictional

torque of the whole setup is aquired including bearing friction (inside cell as well as sensor), churning losses and those of the reference RSS (motor drive sided, not to be analyzed), which must be compensated in the signal. For this purpose, a preliminary test with only the run-in reference RSS mounted serves to determine the aggregated contribution of these effects speed-dependently in order to subtract them as an offset.
To evaluate the general relationship between torque and any negative pressure in the cavity, a test shaft with an external pressure supply was developed for this study as explained in Fig. 4 (right schema).

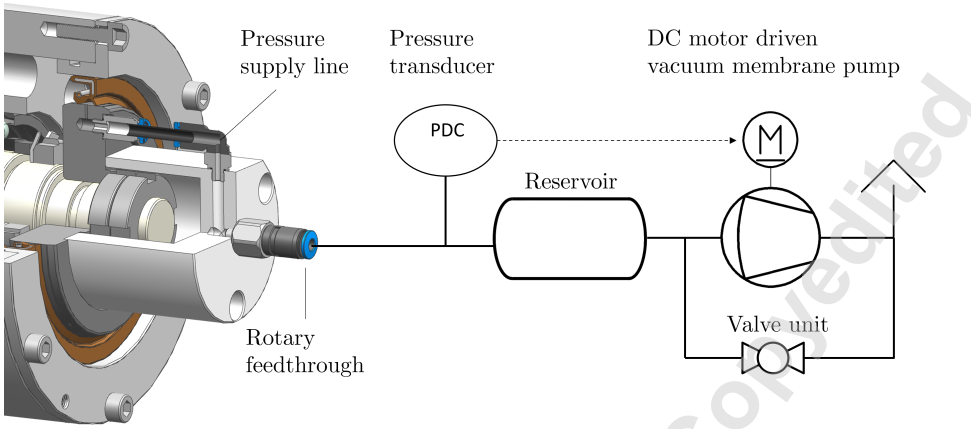

Fig. 4. Test setup for pressurization of the cavity during shaft rotation

The system is connected with the cavity's pressure supply line (c.f. adapter fixed at test shaft shown left in Fig. 4) by a rotary feedthrough and consists of a reservoir, pressure adjusted by a microcontroller-regulated vacuum mebrane pump. Countered by a valved bypass, the pump can regulate pressure at the reservoir outlet operating continuously to an accuracy of $\pm 3,3$ mbar.
Thus the reaction of frictional torque to artificial pressurizations of up to -500 mbar at one specimen can be observed while the cavity of the reference RSS is fully vented (drilled dust lip). By way of the offset compensations described above the measurements deliver insights into the frictional behavior of a single specimen at high underpressures as reached under an instationary shaft movement in the bench test (cf. section 3.1) neglecting all influences of changes in the shaft's rotational direction whose frequency is connected to the seal's central operating parameters like the gap height [2] [17].

2.2 Pressure measurement setup

In order to observe the change of cavity pressure during bench tests due to the pumping effect of both seal lips, without external pressure application, a medical injection cannula connected to a sensor via an Luer adapter piece is inserted into the cavity as shown in Fig. 5, sealing all joints with silicone adhesive.
To evaluate pressure losses occuring at this measurement system, its average inner pressure increase over 72 hours when pressurized to around -400 mbar was determined to be $0,28$ mbar/h. According to DIN 13184:2001-03 for leak tests using the pressure change method [14], this corresponds to a maximum volume loss rate of $0,41$ mm^3/h with respect to the total volume created (cf. Fig. 5) and a calculative reference to the standard condition ($p_\mathrm{N} = 1013,25$ mbar at $T_\mathrm{N} = 0°\mathrm{C}$ [13]) of air which is assumed to be a dry and ideal gas.

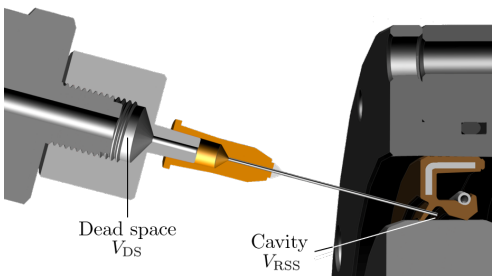

Fig. 5. Section view of total volume (cavity and connected measurement system)

In addition to the volume loss rate mentioned, the measurement system's dead space also influences a negative pressure formation. Due to the enlargement of the cavity V_{RSS} by the dead space V_{DS} as shown in Fig. 5 the pressure reduction rate is reduced. Since due to this a time-based evaluation of the negative pressure formation is not suitable for comparative investigations of the pumping effect occuring at the RSS, a semi-empirical model of the net flow rate based on the measured pressure change was developed for this study. The approach is based on the change in the amount of substance $\frac{dn}{dt}$ (in mol/s) in the measurement system's total volume V_{MS} as a time derivative of the general gas equation (gas constant R) [21].

$$\frac{dn}{dt} = \frac{d}{dt}\left(\frac{p_{\mathrm{i}} V_{\mathrm{MS}}}{R T_{\mathrm{i}}}\right) \tag{1}$$

Here T_{i} as the internal temperature is assumed to be equal to the approximately constant ambient temperature of 20°C due to the uninsulated measurement system (cf. Fig. 5). The internal pressure p_{i} results from the sum of the measured differential pressure p_{d} and the constant ambient pressure $p_{\mathrm{a}} \approx p_{\mathrm{N}}$.
In (1) a pressure-dependent shrinkage of the cavity volume $V_{\mathrm{RSS}}(p_{\mathrm{d}})$ due to elastic deformations is taken into account via empirical relationships according to measurements as described in section 2.3.

$$V_{\mathrm{MS}} = V_{\mathrm{DS}} + V_{\mathrm{RSS}}(p_{\mathrm{d}}) - \varphi_{\mathrm{G}} V_{\mathrm{RSS}}(0\ \mathrm{mbar}) \tag{2}$$

In (2) the approximately constant grease volume is derived from the known degree of greasing φ_{G}. By referring $\frac{dn}{dt}$ to the normal condition of air [13] the net flow rate $\frac{\Delta V}{\Delta t}$ results from the discretized measurement vector as a comparative quantity for an evaluation of the pumping effect occuring at the sealing contact.

$$\frac{\Delta V}{\Delta t} = \frac{R T_{\mathrm{N}} \frac{\Delta n}{\Delta t}}{p_{\mathrm{N}}} \tag{3}$$

Furthermore, since thermal fluctuations are neglected in (1), (2) and (3), the uncertainty they imply for the model must be evaluated. The resulting pressure changes are interpreted by the model as an apparent volume change. If a superposition of this effect with the process of interest is presumed, it can be modeled as an isochoric change of state with analogous assumptions as described above (state ①: $p_{\mathrm{i},1} = p_{\mathrm{d},1} + p_{\mathrm{a}}$ and $T_{\mathrm{i},1} = T_{\mathrm{N}}$; state ②: $p_{\mathrm{i},2} = p_{\mathrm{d},2} + p_{\mathrm{a}}$ and $T_{\mathrm{i},2} = T_{\mathrm{N}} + \Delta T$).

$$p_{\mathrm{d},2} - p_{\mathrm{d},1} = \Delta p_d^{1\to 2} = \frac{\Delta T}{T_{\mathrm{N}}}(p_{\mathrm{a}} + p_{\mathrm{d},1}) \tag{4}$$

Since (4) makes clear that the effect of thermally induced pressure fluctuations grows by $p_{\mathrm{d},1}$, its maximum value 0 mbar is used here in the sense of a worst-case estimation, which leads to a pressure rise of $\Delta p_d^{1\to 2}$ / ΔT = 3.46 mbar/°C. By multiplication with both, the highest observable heating and cooling rate taken from several days of room temperature monitoring, the rates of pressure change are obtained which lead to maximum error of $[-1,89; +2,52]$ mm^3/h according to (1), (2) and (3).

2.3 Setup for geometry measurement with controlled underpressure

Since already moderate negative pressures from −200 mbar prevailing constantly in the cavity are considered to impair a seal lip's contact situation significantly [7] the specimen's vacuum-induced elastic deformation in a static case was characterized using an optical measuring device typically used for determining wear based on the measurement of geometric changes (Wear-Tester) [12]. As illustrated by an exemplary setup in Fig. 6, the reflection of a laser line deflected by a plan mirror onto the RSS is recorded by a CCD array sensor, delivering both a gray image and a height profile of specimen and the fixture's reference diameter.

Journal of Tribology. Received April 13, 2023;
Accepted manuscript posted September 19, 2023. doi:10.1115/1.4064511

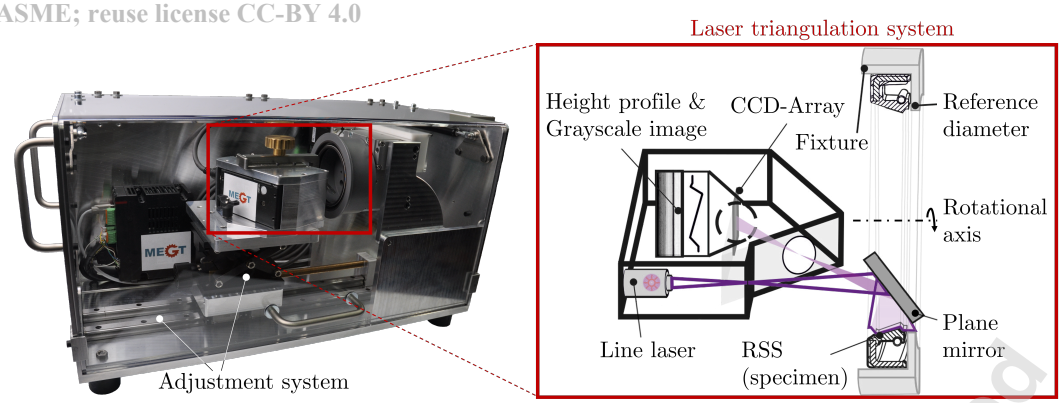

Fig. 6. Setup and functional principle according to BURKHART [12] of Wear-Tester for circumferential profile measurement

By rotating specimen and fixture the entire circumference is scanned analogously for a subsequent automated determination of various geometric parameters.
For profile measurements of an RSS at the negative pressure levels observed in the bench tests, the device is extended by the same microcontroller-regulated pumping system, explained before (c.f. Fig. 4). Joined via a rotary feedthrough, the pressure supply line is routed to the cavity of the RSS, which is mounted on an acrylic glass hollow shaft (outer diameter 80 mm) as shown in Fig. 7.

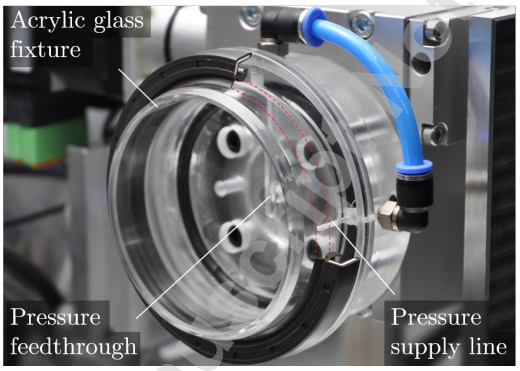

Fig. 7. Measurement through transparent fixture

The pressure-dependent reaction of the assembly geometry measured in the shown setup is characterized by formation of several geometric parameters, as described by way of example in Fig. 8. An indicator for macrogeometric deformation is provided by the size of the cavity as a volume integration over all profile measurements. This parameter also provides the empirical relationship between differential pressure and profile contraction $V_{\mathrm{RSS}}(p_{\mathrm{d}})$ as implemented in the net flow rate model in section 2.2. Major changes in the shape of the main lip are detected by calculating the contact angles. Since a contact area cannot be resolved in the profile measurements (cf. highlighted regions in Fig. 8) due to restrictions in the measurement principle, here the flanks are extrapolated using a secant fit method.

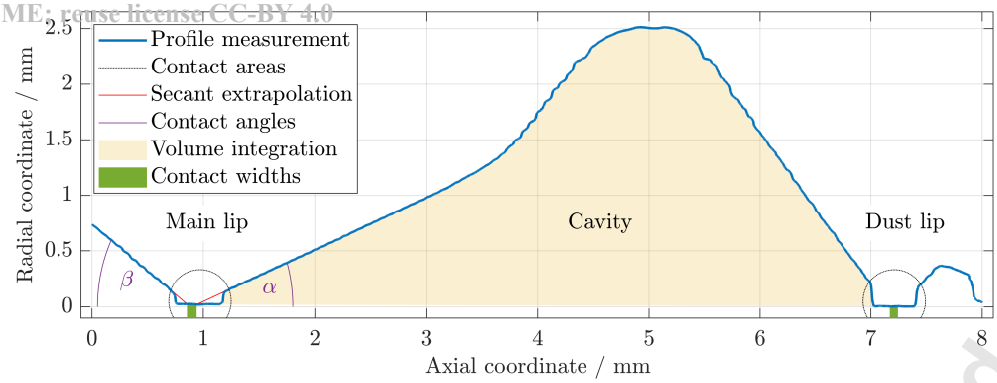

Fig. 8. Characteristic geometric parameters on exemplary single profile measurement

In order to evaluate deformations on the microscopic scale with direct influence on the sealing contact the main lip's contact width b_{ML} is also approximated from the profile measurement using both the fitted secants and the grayscale image captured during the measurement [12]. Due to its more complex geometry, the dust lip's contact width b_{DL}, on the other hand, is exclusively determined from the grayscale image.

2.4 Simulation model

Since the contact parameters obtained from the optical measurement described in section 2.3 can neither provide information about the system's behavior at operating conditions nor about the axial contact pressure distribution, which is essential for estimating the intensity of the sealing mechanism (compare section 1), those insights are provided by a simulative investigation. The approach used is based on existing concepts for an axisymmetric assembly simulation [15] [16] in adaptation to seal designs with a contacting dust lip at a cavity pressurization.
Therefore a finite elements (FE) mesh is derived from a micrograph of the unassembled RSS molded in synthetic resin with a removed garter spring analogously to the experimental setup.

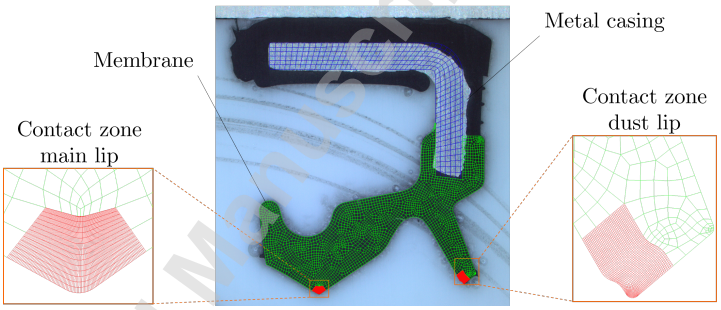

Fig. 9. Mesh generation in RSS contour captured from micrograph

The macrogeometric contour is captured manually from the cross section as shown in Fig. 9, while both seal edge radii are obtained from profile measurements. During subsequent discretization, the mesh resolution is locally adjusted to expected stresses and deformations. Additional refinements in the contact zones further enable the contact pressure curves' extraction in a high resolution (compare wireplot details in Fig. 9, element size $\approx 10^{-6}$ m).
As illustrated in Figure 10, a simulation starts with mounting the fixed RSS on the shaft by its axial displacement. Subsequently the entire system is heated to the homogeneous operating temperature until a constant line load on the cavity contour bordered by the contact zones performs the pressurization. In this last simulation step, the previously tangential frictionless contact behavior between rubber and shaft is replaced by the adhesion condition.
Since the implemented hyperelastic material model represents the long-term behavior of the fluoroelastomer used, any further relaxation steps are omitted in the simulation process [15].

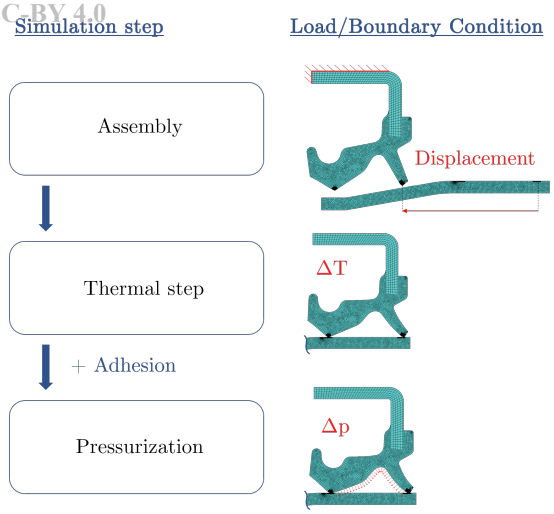

Fig. 10. Simulation setup

2.5 Measurement regime

Since the presented study is motivated by application scenarios with high demands on the reliability of the sealing system (compare section 1.1) the experimental investigation is performed on parameters related to the food processing industry that are considered to be particularly critical in terms of leak tightness [8].
Test specimen are RSS (DIN3760-AS80x100x10-FKM [22]) with a contacting dust lip at a high degree of greasing inside the cavity $\varphi_G = 46 \pm 7\%$. As well as the grease, the polyglycol-based gear oil (ISO 3448 viscosity class 220 [23]), which entirely fills the test cell at a controlled temperature of 60°C, is designed for use in food as well as pharmaceutical production plants. As a countersurface rolled test shafts (outer diameter 80 mm) perform an instationary movement profile $\phi(t)$ shown in Fig. 11. At each reversal points of the triangular 7 Hz profile accelerations of 7.000 rad/s^2 are enforced, causing deviations from the control signal (cf. Fig. 11)

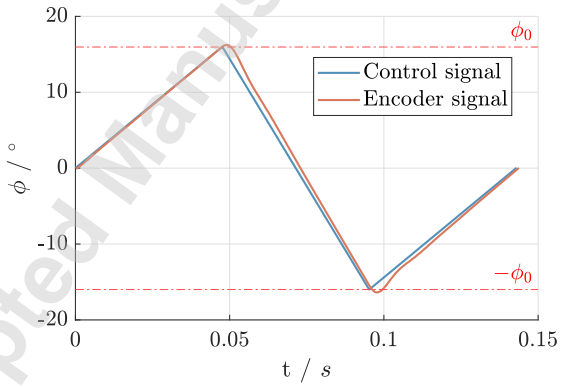

Fig. 11. Triangular movement profile

Since in addition to a characterization of the negative pressure build up based on the initial net flow rate (cf. section 2.2) and its long-term behavior, its connection with highly dynamic changes in the rotational direction is also to be evaluated (section 3.1), reference values are obtained by an analogous test setup with a constant speed of 75 rpm (sliding velocity 300 mm/s) which corresponds to the average rotational speed of the instationary movement profile.
Furthermore, using the test setup for artificial pressurization described in section 2.1, the influence of pressure on frictional torque in general is investigated at the same configuration (section 3.2).

3 Results

3.1 System behaviour under instationary shaft movement

As presumed from previous investigations on the leakage behavior of RSS under instationary shaft movement [8], significant build ups of negative pressure can be observed in the bench tests. The exemplary pressure drop shown in Figure 12 beginning immediately after start-up proceeds continuously until a minimum of −347 mbar is reached after 155 h, disregarding a breakpoint caused by failure of the temperature control (compare sump temperature after 80 h in Fig. 12).

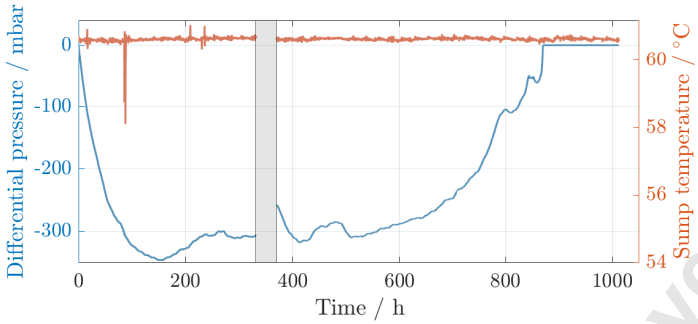

Fig. 12. Exemplary pressure course in high dynamic bench test (pause highlighted in gray)

After this minimum is sustained constantly except for fluctuations during a hold time of about 300 h the pressure level is shifted up to a complete pressure equalization after 870 h without any appearance of leakage.
This pressure course, consisting from the phases of build up, hold time and pressure equalization, can be observed equally in a repeated long term test, whereby the negative pressure reached (−270 mbar) as well as the duration until its equalization (> 2000 h) differ. The characteristic behavior described will be analyzed in detail below.

Evolution of underpressure

According to section 2.2 the seal's pumping effect, which is considered to be responsible for the evacuation process, can be characterized by its initial pressure-dependent net flow rate. For this purpose Figure 13 provides a comparison of the net flow rates according to section 2.2 over pressure from start-up until reaching the pressure minimum. The data is calculated from the pressure course shown in Fig. 12, a repeated bench test carried out at another test cell and a reference test at the constant shaft speed of 75 rpm (compare section 2.5).

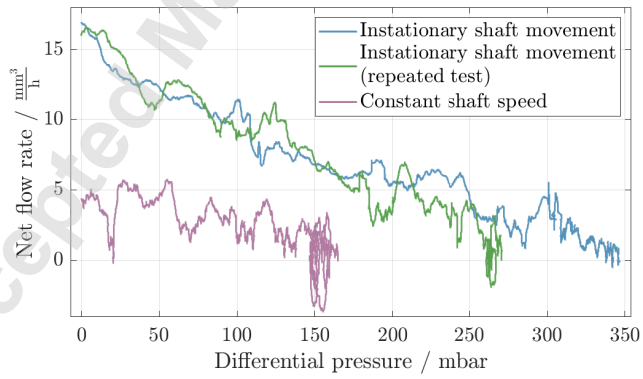

Fig. 13. Comparison of net flow rates over pressure from start-up (0 mbar) to pressure minimum (zero crossing)

Regardless of the type of shaft movement, here the net flow rate is affected by a strong decrease starting from a maximum at the beginning (0 mbar), which implies a pressure-dependency of the sealing mechanisms in general. Presumably the global pressure gradient opposes flows directed out of the cavity and supports compensatory flows such as at the measurement system due to air leakage. Furthermore, as known from literature, the flow rate occuring at a sealing contact can be influenced

by a pressure-induced change in contact load [1] [18] [26]. In addition, changes in contact parameters due to the RSS's elastic deformation (cf. section 3.2) can have a major pressure-dependent influence on the sealing mechanisms.
While the net flow rates at both instationary tests in Fig. 13 show a good accordance besides a scattering in the achieved minimum pressure, the reference test with stationary shaft rotation results in significantly lower net flow rates at each pressure level. Since both types of shaft movement bring the same average sliding velocity, it is to be assumed that the pumping effect is increased by high-frequency changes in the rotational direction. However, the underlying physical causes cannot yet be determined by examinations of the net flow rate.

Holding time and pressure equalization

Following Figure 13 the net flow rate decreases during the evacuation process up to a zero crossing reaching the pressure minimum, which is held almost constantly in the following. Particulary striking in the course of Figure 12 is that even after pausing the bench test, the previous pressure level is reached again during a second start-up (400 h). This system behavior could be clearly reproduced in a repeated bench test as shown in Figure 14 by venting the cavity manually lifting the dust lip after 200 h of operation for a subsequent restart.

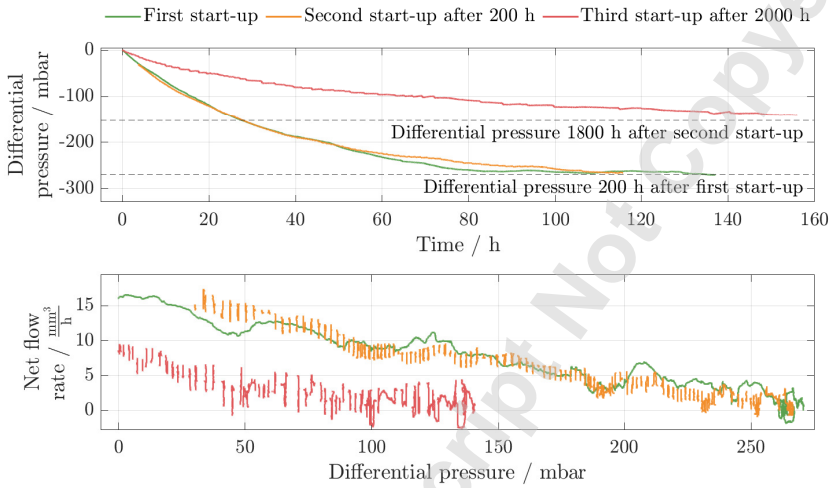

Fig. 14. Differential pressure/pressure-dependent net flow rate over time at multiple start-ups in repeated bench test (each plot showing the pressure drop until minimum reached)

Here, the constant pressure level prevailing before shutdown is also reached again, whereby a noticeable agreement in the time- and pressure-dependent pumping behavior can be observed except for disturbances in the pressure signal occurring during the second start-up (compare incontinuities in net flow rate of Fig. 14). These observations lead to the assumption that the constant minimum pressure appears as an equilibrium between the individual flows at main and dust lip as well as additional volume losses (eg. at the measurement system according to section 2.2).
According to Figure 14 a second repeated start-up from 0 mbar after 1800 h, when the differential pressure had already been reduced to 150 mbar, also leads to the pressure level before venting being reached again. At this third vacuum build up in addition to the minimum pressure the net flow rate is significantly lower compared to the first two startups. Consequently for losses of negative pressure as observed in the long-term test of Fig. 12 the minimum's stable operation point must be shifted upwards by changes in the pumping performance of one or both sealing contacts. Since after all tests no oil leakage could be detected inside the cavity, the resulting pressure equalization must have been taken place at the dust lip. As a cause for this, analyses of the lip contours as well as the prevailing contact width (obtained from profilometric measurements described in section 2.3) and radial force (measured following the two-jaw method according to DIN 3761-9:1984-01 [32]) at room temperature shown in Figure 15 suggest progressive wear.

Journal of Tribology. Received April 13, 2023;
Accepted manuscript posted September 19, 2023. doi:10.1115/1.4064511

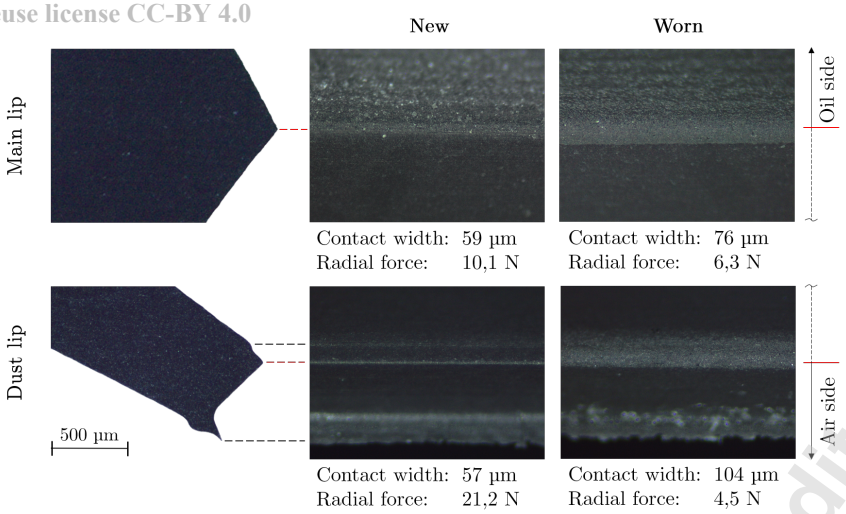

Fig. 15. Comparison of new and worn (> 1000 h instationary shaft movement) seal edges by microscopic images and corresponding contact width (based on profilometric measurements, see section 2.3) as well as radial force (determined according to DIN 3761-9:1984-01 [32]) at room temperature in the non-pressurized state

Comparing the microscopic images before and after the long-term test of Figure 12, the consequences of abrasive wear are noticeable in both contact areas, with the change in shape at the dust lip predominating. While the contact width, as determined with the methods of chapter 2.3, of the main lip increases by 29% over about 1000 h of instationary shaft rotation, it enlarges by more than 83% at the dust lip, which is accompanied by decreases in the prevailing radial force of 38% at the main lip and 79% at the dust lip. Wear-induced net flow reductions could thus originate from increasing compensatory currents at the dust lip as a result of its potentially impaired follow-up capability at each reversal point of the triangular movement profile. In addition, leakage channels in the sealing contact have been shown to open and close depending on the direction of rotation [28]. Furthermore, based on the sealing hypotheses (cf. sec. 1), the pumping effect itself is expected to be influenced by the interaction of wear, pressure load and also contact temperature [29]. A possible reversion of the flow direction at the dust lip by reshaping the pressure distribution on its increasing contact width [27] could therefore contribute equally to the pressure equalization process (cf. sec. 3.2).
Since the vacuum build up is focused in this study, the pressure dependence of the contact parameters associated with pumping mechanisms is examined in the following section 3.2. Considerations of correlations of wear with the pressure equalization or potential oil leakage must therefore be subject of future research.

3.2 Influence of underpressure on contact situation

According to section 3.1, instationary shaft movements support formations of high negative pressures in the cavity. As a result, the elastomer part is subjected to elastic deformation, which can be characterized using the geometric contact parameters described before (cf. sec. 2.3).
A selection of these, captured from simulations (cf. section 2.4) and optical measurements (cf. section 2.3) of an unworn RSS are therefore plotted in Figure 16 in dependence on differential pressure up to -400 mbar.

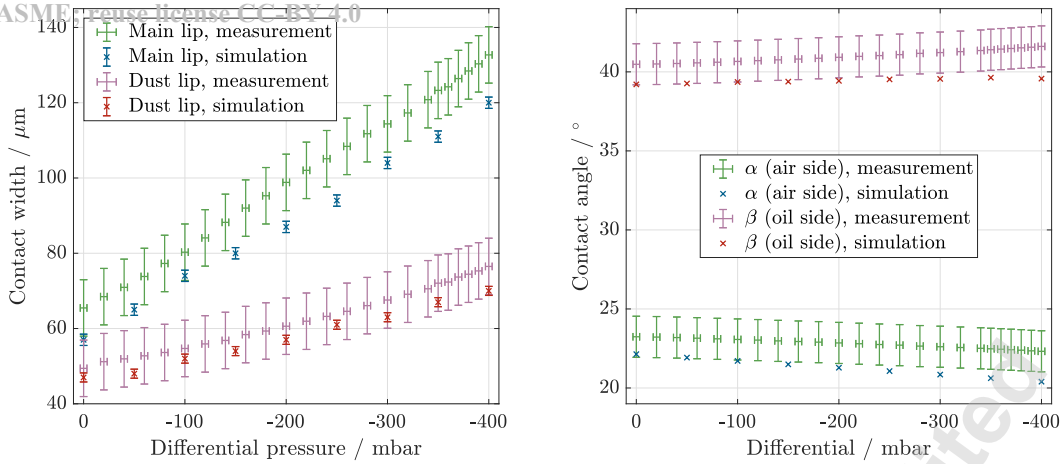

Fig. 16. Pressure-dependent contact widths and contact angles at main lip from optical measurements and simulation (new RSS at room temperature); worst-case error of measurements (origin: maximum contact width and contact angle variation at given RSS batch) and simulation (origin: discretization level) each represented by error bars

Here, during lowering the cavity pressure a continuous shift of the main lip's contact angles (right diagram) becomes apparent, whereby the air side angle α decreases in the same pressure-dependent amount as the oil side angle β increases. Furthermore, a noticeable growth of both contact widths (left diagram) with nearly linear behavior is demonstrated by both approaches, with an increase at the main lip exceeding that at the dust lip. The growth's direction becomes visible from displacements of the contact width limits found during the optical measurement, as exemplified in Figure 17.

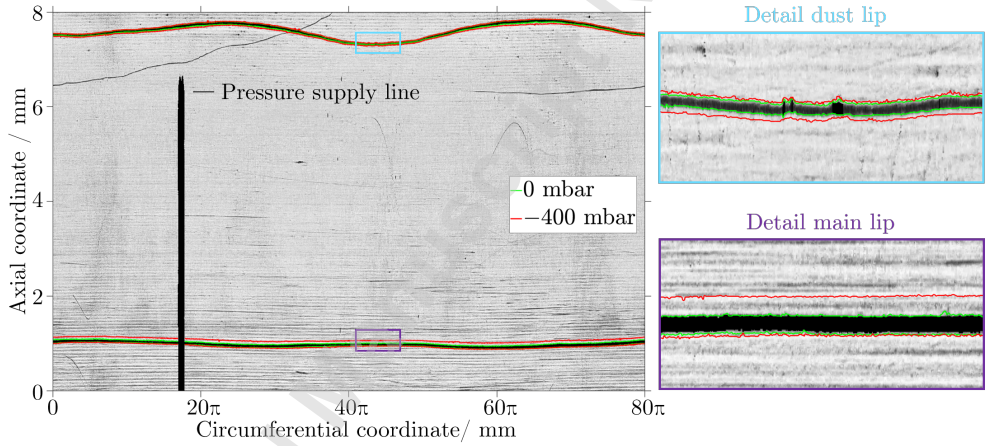

Fig. 17. Shift of contact area limits due to pressurization (new RSS at room temperature) inserted in gray image of optical measurement captured at differential pressure 0 mbar

As shown, the main lip's contact width expands predominantly toward the cavity, which is due to a tilting toward the air side accompanied by a lowering of the membrane. This rotational movement involves small component of macrogeometric deformation around the seal edge, as indicated from the inverse contact angle shift of Fig. 16. At the dust lip a similar deformation behavior occurs, but is much less pronounced due to its different geometry as well as proximity to the stiffening metal casing.

According to the simulation results, at operating temperature (60°C) the RSS also reacts to a pressurization as described above (room temperature), intensifying all deformation mechanisms presented due to a more flexible material behavior. Therefore pressure-induced changes of flow rates must be expected during operation, since contact angle displacements in particular affect the axial pressure distribution between RSS and shaft, which is responsible for the pumping effect (cf. sec. 1).

Fig. 18 shows the contact pressure distribution in both contact areas at pressure equalization as well as the highest experimentally observed differential pressure, in each case at operating temperature. In addition to growing contact widths, a

Journal of Tribology. Received April 13, 2023;
Accepted manuscript posted September 19, 2023. doi:10.1115/1.4064511

significant increase of contact pressure at both lips is striking. Contributing to its premature wear (cf. sec. 3), the dust lip here is comparatively subjected to a much higher load at each pressure level.

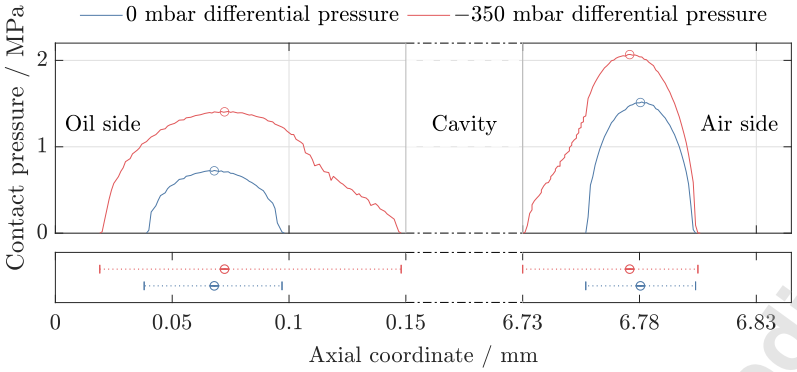

Fig. 18. Simulated axial contact pressure distributions of main lip (left) and dust lip (right) at $60°C$ and differential pressures of 0 mbar as well as -350 mbar / -0.035 MPa with contact width proportions visualized below for each case

Furthermore, insights into the pressure-dependent dynamic sealing mechanism can be obtained from the contact pressure distributions. According to the distortion principle, which is largely considered to be responsible for an inward pumping [25], due to an imprint of this load profile into the shear stress distribution during shaft rotation the rubber's roughness pattern is stretched and disorted into a V-shape [1] [25]. By this structure fluid is deflected axially toward the pressure maximum from both sides based on the screw pump principle, with the flow direction of the larger contact width proportion dominating [4]. The validity of this hypothesis has not yet been proven for instationary shaft rotations, but the underlying asymmetric distortion of the elastomeric contact topography could already be demonstrated in the sliding phases of a triangular movement profile [20]. According to Fig. 18, the contact width proportions left as well as right sided of each maximum change pressure-dependently. Additionally, at rising underpressures there are increasing deviations of both contact pressure curves from their characteristic shape, which, however, is a prerequisite for the distortion principle. As a consequence for the presented study, the pressure curve's shape deviation is taken into account by integrating it on both sides of the maximum, as schematically illustrated in Fig. 19.

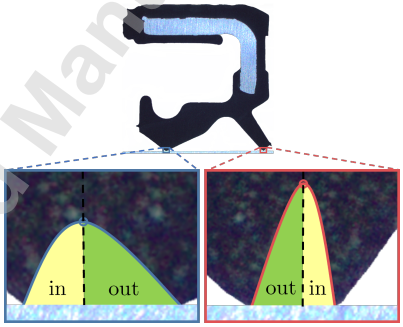

Fig. 19. Radial force proportions supporting inward and outward flow as contact pressure integrations left and right side of maximum

Assuming that the two resulting radial force proportions correlate to the sealing mechanism in the same way, the ratio of these (outward divided by inward proportion) can be interpreted as an indicator for flow direction and -strength of a contact. According to Fig. 18, a radial force ratio higher than 1 would thus support the flow directed out of the cavity and inversely for smaller values. Fig. 20 shows the radial force ratio as a function of differential pressure for both contacts.

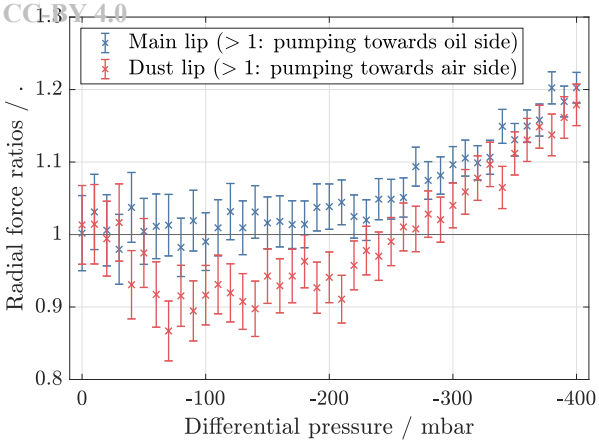

Fig. 20. Pressure-dependent radial force ratios from simulation with worst case propagation of dicretization error marked as error bars

Its course at the main lip, neglecting some scattering within the error range, implies a constant flow direction toward the oil side reaching a self-reinforcement mechanism at higher pressure differences. At the dust lip, on the other hand, a minimum occurs in the radial force ratio already at a low pressure difference, indicating a potential reversal of the pumping direction. Thus, the pressure minimum of about −150 mbar (cf. Fig. 13) observed at the bench test under constant shaft speed can be suspected to be caused by an inward pumping of the dust lip leading to the equilibrium state. If this state gets exceeded, such as due to strengthened pumping mechanisms by instationary shaft movement, the dust lip's radial force ratio reverts again. Above this point, as at the main lip, a sharp increase follows, further supporting the negative pressure build up.

Some reasons for the appearance of a net flow equilibrium in the dynamic case, which are potentially interacting with each other (discussed in sec. 3.1), can not be displayed by the simulation model presented. However, as one of the causes for this pressure build up limitation an increase in radial force can be found in the simulation, which in both contact areas behaves proportionally to the differential pressure. On reaching the pressure minimum (−350 mbar according to sec. 3.1), the total radial force as the sum over both contacts almost triples, as shown in Fig. 21 (right ordinate). As a result, measurements of the frictional torque under controlled pressurization (cf. sec. 2) at low, constant shaft speed (left ordinate, 5 rpm) show an increase in the frictional torque to the same pressure-dependent extent. At higher speeds, such as those of the reference test (left ordinate, 75 rpm), frictional torque without pressurization initially increases due to a rising contribution of viscous friction [31]. Since this proportion of the total frictional torque depends, among other factors, on the contact width [1] [2] [31], an application of differential pressures to this operational state even results in superproportional growth.

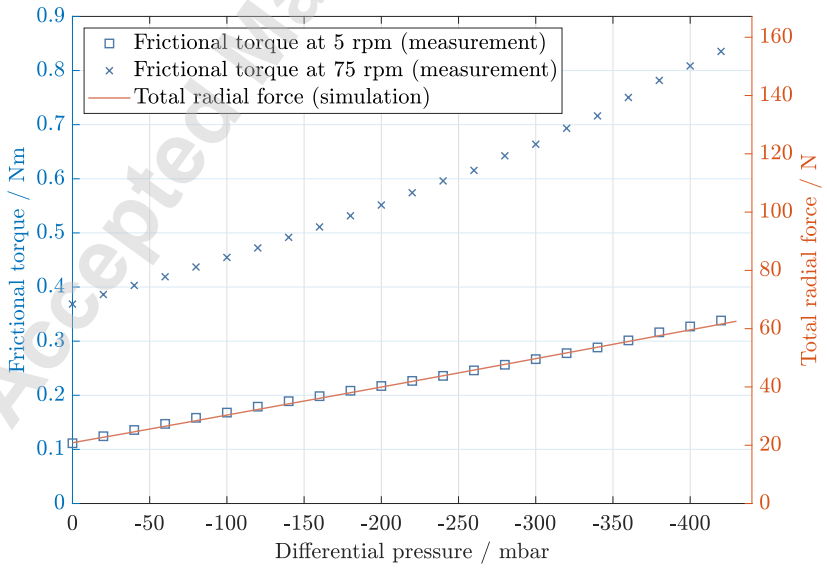

Fig. 21. Pressure-dependent frictional torque measured at different constant shaft speeds in correlation to total radial force (sum of main and dust lip, simulation) at 60°C

Although analogous investigations have not yet been carried out in the dynamic case, similarly severe impacts of the negative pressure on the frictional torque can be expected there as well. Thus, instationary shaft movement not only compromise the functional reliability of an RSS by still unknown leakage mechanisms, but also its operational efficiency and durability.

4 Conclusion and outlook

At RSS with a contacting dust lip under instationary shaft movement, changes in the operational behavior are held responsible for frequent occurrence of leakage in industrial applications. Therefore experimental investigations were carried out within the presented study. In the bench tests, a significantly accelerated vacuum build up inside an RSS's cavity due to instationary shaft movement in comparison to a constant shaft speed was demonstrated. Regardless of the type of shaft movement the sealing system thereby strives for a net flow neutral operation point. At constant shaft speed this stable state is reached at a lower differential pressure level, whereby an equilibrium between the individual pumping effects at both contacts is suggested as a potential cause due to a simulative consideration. When this operation point is exceeded, possibly by a strengthening of pumping mechanisms due to instationary shaft movement, a self-reinforcement mechanism is suspected, encouraging the formation of higher negative pressures.

As a consequence central operational parameters of the sealing system are severly affected. In addition to significant changes in geometrical contact parameters the experimentally generated pressure levels also cause a major superelevation of both radial forces and hence friction losses. Thus it will be important to limit the negative pressure build up in the interests of efficiency in the future.

Furthermore, pressure-induced rapidly progressive wear was observed at the dust lip, up to its loss of function, which led to permanent pressure equalization between cavity and air side. Some leakage occurrences in industrial applications with contaminated environments might therefore be due to consequential damage caused by premature dust lip failure. However, since previous investigations have shown that leakage can occur even under laboratory conditions after short runtimes [8] and is considered to be a result of the dynamics, the behavior of RSS at instationary shaft movement must still be better understood in order to explain failures. For this purpose, an extension of the presented static simulation approach could serve to determine, to what extend potential losses of the RSS's follow-up capability in the reversal points of a movement profile affect its net flow rate or even tightness. Since the present study also identified vacuum-induced deformations and wear as processes with a direct influence on the pumping effect, it is important to estimate their critical interaction in the course of the simulative consideration as well.

According to the current state of research, the underlying physical mechanisms effecting increased net flow rates during instationary shaft movement are not known. These can neither be localized nor explained yet by the approaches of the presented study. Observations of the individual pressure-dependent flow rates at both contact areas, as well as the simulation of the sealing contact on a microscopic scale, must thus help to further improve our knowledge of system behavior in order to enhance the sustainability of RSS under highly dynamic conditions in the future.

References

[1] Flitney, R. K., 2014. *Seals and Sealing Handbook*, 6 ed. Butterworth-Heinemann, June.

[2] Thielen, S., Magyar, B., and Sauer, B., 2020. "Thermoelastohydrodynamic lubrication simulation of radial shaft sealing rings". *Journal of Tribology,* **142**(5), jan.

[3] Salant, R. F., and Flaherty, A. L., 1995. "Elastohydrodynamic analysis of reverse pumping in rotary lip seals with microasperities". *Journal of Tribology,* **117**(1), jan, pp. 53–59.

[4] Mueller, H. K., 1998. *Fluid sealing technology*, Vol. 117 of *Mechanical Engineering*. M. Dekker, June.

[5] Salant, R. F., 1999. "Theory of lubrication of elastomeric rotary shaft seals". *Proceedings of the Institution of Mechanical Engineers, Part J: Journal of Engineering Tribology,* **213**(3), mar, pp. 189–201.

[6] Flitney, R. K., 2013. "Rotary shaft lip seals". *Encyclopedia of Tribology*, pp. 2947–2954.

[7] Peisker, G., and Sahiouni, J., 1989. "Performance of various shaft seal dust lips in a dust environment and their ability to form a vacuum between the primary and secondary lips". *SAE Transactions,* **98**, pp. 266–272.

[8] Thielen, S., Aghdasi, A., and Sauer, B., 2020. "Leakage prevention for radial shaft seals used in instationary conditions". *Konstruktion,* **2020**(07-08), pp. 68–74.

[9] EFSA, 2012. "Scientific opinion on mineral oil hydrocarbons in food". *EFSA Journal*.

[10] foodwatch International, 2021. "Toxic mineral oil in food - laboratory tests 2021". *Foodwatch, december 2021*.

[11] Centre., E. C. J. R., 2019. *Guidance on sampling, analysis and data reporting for the monitoring of mineral oil hydrocarbons in food and food contact materials.* Publications Office.

[12] Schollmayer, T., Burkhart, C., Kassem, W., Thielen, S., and Sauer, B., 2021. "Verschleißanalyse an Radialwellendichtringen und weiteren Maschinenelementen mittels Laserprofilometrie". *Gesellschaft für Tribologie e.V. (Hg.): 62. Tribologie-Fachtagung,* **62**, pp. 70/1–70/10.

[13] DIN 1343:1990-01, reference conditions, normal conditions, normal volume; concepts and values.

[14] DIN EN 13184:2001-07, non-destructive testing - leak test - pressure change method; german version EN 13184:2001.

[15] Frölich, D., Magyar, B., and Sauer, B., 2014. "A comprehensive model of wear, friction and contact temperature in radial shaft seals". *Wear,* **311**(1-2), mar, pp. 71–80.

[16] Burkhart, C., Weyrich, D., Thielen, S., Schollmayer, T., and Sauer, B., 2021. "Development and optimization of a tribometer for radial shaft seals". *Journal of Tribology,* **143**(4), feb.

[17] Eipper, A., 2018. *Einfluss transienter Betriebsbedingungen auf den RWDR im System Radial-Wellendichtung*. PhD thesis, Universitat Stuttgart.

[18] Wollesen, V., and Förster, K., 2002. "Auswirkung eines geringen, stirnseitig erzeugten unterdrucks auf den dichtzonenbereich und das betriebsverhalten von rwdr". In 12th International Sealing Conference, VDMA e.V., Fachverband Fluidtechnik im VDMA e.V., pp. 141–155.

[19] Mueller, H. K., 1990. *Abdichtung bewegter Maschinenteile*. Medienverlag Ursula Müller.

[20] Klüppel, M., and Poll, G., 2020. Verbesserung der Verschleißfestigkeit von Radialwellendichtungen im oszillierenden Reibkontakt, Schlussbericht zu IGF-Vorhaben Nr. 19280. Tech. rep., Deutsches Institut für Kautschuktechnologie e.V.

[21] Moran, M. J., Shapiro, H. N., Boettner, D. D., and Bailey, M. B., 2014. *Fundamentals of Engineering Thermodynamics*, 8 ed. Wiley.

[22] DIN 3760:1996-09, rotary shaft lip type seals.

[23] DIN ISO 3448:2010-02, industrial liquid lubricants - ISO viscosity classification (ISO 3448:1992).

[24] Kammüller, M., 1986. *Zum Abdichtverhalten von Radial-Wellendichtringen*, Vol. Nr. 20 of *Institutsbericht*. PhD thesis, Universitat Stuttgart. 49.

[25] Baart, P., Lugt, P. M., and Prakash, B., 2009. "Review of the lubrication, sealing, and pumping mechanisms in oil- and grease-lubricated radial lip seals". *Proceedings of the Institution of Mechanical Engineers, Part J: Journal of Engineering Tribology,* **223**(3), jan, pp. 347–358.

[26] Ottink, K., 2014. *Betriebsverhalten von Wälzlagerschutzdichtungen: Experimentelle Untersuchungen und Berechnungsansätze*. PhD thesis, Universitat Hannover.

[27] Guo, F., Jia, X., Longke, W., Salant, R. F., and Wang, Y., 2014. "The effect of wear on the performance of a rotary lip seal". *Journal of Tribology,* **136**(4), jun.

[28] Schulz, M., Hagmayer, M., Baumann, M., and Bauer, F., 2021. "Analysis of fluid flow in the sealing gap of radial shaft seals and elastic deformation of the sealing surface". *Journal of Tribology,* **143**(12), mar.

[29] Kang, Y. S., and Sadeghi, F., 1997. "Numerical analysis of temperature distribution at the lip seal-shaft interface". *Journal of Tribology,* **119**(2), apr, pp. 273–278.

[30] Foko, F. F., Heimes, J., Magyar, B., and Sauer, B., 2020. "Friction energy-based wear simulation for radial shaft sealing ring". *Lubricants,* **8**(2), feb, p. 15.

[31] Wennehorst, B., Engelke, T., and Poll, G., 2011. "Modelling radial lip seal friction - a multi-scale mixed lubrication approach". In 21st International Conference on Fluid Sealing.

[32] DIN 3761:1984-01, rotary shaft lip type seals for automobils; test; radial force measuring instrument digital.

5 List of figure captions

Figure 1: Cross section of an assembled radial shaft seal with dust lip

Figure 2: High acceleration test bench

Figure 3: Section view of a test cell

Figure 4: Test setup for pressurization of the cavity during shaft rotation

Figure 5: Section view of total volume (cavity and connected measurement system)

Figure 6: Setup and functional principle according to BURKHART [12] of Wear-Tester for circumferential profile measurement

Figure 7: Measurement through transparent fixture

Figure 8: Characteristic geometric parameters on exemplary single profile measurement

Figure 9: Mesh generation in RSS contour captured from micrograph

Figure 10: Simulation setup

Figure 11: Triangular movement profile

Figure 12: Exemplary pressure course in high dynamic bench test (pause highlighted in gray)

Figure 13: Comparison of net flow rates over pressure from start-up (0 mbar) to pressure minimum (zero crossing)

Figure 14: Differential pressure/pressure-dependent net flow rate over time at multiple start-ups in repeated bench test (each plot showing the pressure drop until minimum reached)

Figure 15: Comparison of new and worn ($>$ 1000 h instationary shaft movement) seal edges by microscopic images and corresponding contact width (based on profilometric measurements, see section 2.3) as well as radial force (determined according to DIN 3761-9:1984-01 [32]) at room temperature in the non-pressurized state

Figure 16: Pressure-dependent contact widths and contact angles at main lip from optical measurements and simulation (new RSS at room temperature); worst-case error of measurements (origin: maximum contact width and contact angle variation at given RSS batch) and simulation (origin: discretization level) each represented by error bars

Figure 17: Shift of contact area limits due to pressurization (new RSS at room temperature) inserted in gray image of optical measurement captured at differential pressure 0 mbar

Figure 18: Simulated axial contact pressure distributions of main lip (left) and dust lip (right) at 60°C and differential pressures of 0 mbar as well as -350 mbar / -0.035 MPa with contact width proportions visualized below for each case

Figure 19: Radial force proportions supporting inward and outward flow as contact pressure integrations left and right side of maximum

Figure 20: Pressure-dependent radial force ratios from simulation with worst case propagation of dicretization error marked as error bars

Figure 21: Pressure-dependent frictional torque measured at different constant shaft speeds in correlation to total radial force (sum of main and dust lip, simulation) at 60°C